# Anisotropic ultraviolet-plasmon dispersion in black phosphorus

| | |
|---|---|
| Journal: | *Nanoscale* |
| Manuscript ID | NR-ART-07-2018-005502.R1 |
| Article Type: | Paper |
| Date Submitted by the Author: | 29-Sep-2018 |
| Complete List of Authors: | Nicotra, Giuseppe; CNR-IMM,<br>van Veen, Edo; Radboud Universiteit, Theory of Condensed Matter<br>Deretzis, Ioannis; CNR-IMM, Catania,<br>Wang, Lin; Shanghai Institute of Technical Physics, Chinese Academy of Sciences, National Laboratory for Infrared Physics<br>Hu, Jin; Tulane University, Physics and Engineering Physics<br>Mao, Zhiqiang; Tulane University, Department of Physics and Engineering Physics<br>Fabio, Vito; Università della Calabria, Fisica<br>Spinella, Corrado; Consiglio Nazionale delle Ricerche,<br>Chiarello, Gennaro; Università degli Studi della Calabria, Fisica<br>rudenko, alexander; Radboud Universiteit Institute for Molecules and Materials<br>Yuan, Shengjun; Radboud University of Nijmegen, Institute for Molecules and Materials<br>Politano, Antonio; Istituto Italiano di Tecnologia |
| | |

# Anisotropic ultraviolet-plasmon dispersion in black phosphorus

Giuseppe Nicotra[1,§,*], Edo van Veen[2,3,§], Ioannis Deretzis[1], Lin Wang[4,5], Jin Hu[6,7], Zhiqiang Mao[8], Vito Fabio[9], Corrado Spinella[1], Gennaro Chiarello[9.*], Alexander Rudenko[2,3*], Shengjun Yuan[2,3,*], Antonio Politano[10,11*]

[1] *Istituto per la Microelettronica e Microsistemi (IMM-CNR), VIII Strada 5, I-95121 Catania, Italy*

[2] *School of Physics and Technology, Wuhan University, Wuhan 430072, China*

[3] *Institute for Molecules and Materials, Radboud University, Heijendaalseweg 135, NL-6525 AJ Nijmegen, The Netherlands*

[4] *State Key Laboratory of Infrared Physics, Shanghai Institute of Technical Physics, Chinese Academy of Sciences, Shanghai, China*

[5] *Synergetic Innovation Center of Quantum Information & Quantum Physics, University of Science and Technology of China, Hefei, Anhui, China*

[6] *Department of Physics, University of Arkansas, Fayetteville, Arkansas 72701, United States*

[7] *Institute for Nanoscience and Engineering, University of Arkansas, Fayetteville, Arkansas 72701, United States*

[8] *Department of Physics and Engineering Physics, Tulane University, New Orleans, Louisiana 70118, United States*

[9] *Department of Physics, University of Calabria, via ponte Bucci, cubo 31C, 87036 Rende (CS), Italy*

[10] *Fondazione Istituto Italiano di Tecnologia, Graphene Labs, via Morego 30, 16163 Genova, Italy*

[11] *Department of Physical and Chemical Sciences, University of L'Aquila, via Vetoio, 67100 L'Aquila, Italy*

§ These authors have equally contributed

Abstract

By means of momentum-resolved electron energy loss spectroscopy (EELS) coupled with scanning transmission electron microscopy, we have studied the dispersion relation of interband plasmonic modes in the ultraviolet in black phosphorus. We find that the dispersion of the interband plasmons is anisotropic. Experimental results are reproduced by density functional theory, by taking into account both the anisotropy of the single-particle response function, arising from the anisotropic band structure, and the damping. Moreover, our theoretical model also indicates the presence of low-energy excitations in the near-infrared that are selectively active in the armchair direction, whose existence has been experimentally validated by high-resolution EELS (HREELS) in reflection mode.

*corresponding authors

e-mail: giuseppe.nicotra@imm.cnr.it; gennaro.chiarello@fis.unical.it; a.rudenko@science.ru.nl; s.yuan@whu.edu.cn; antonio.politano@iit.it,

# 1 Introduction

Recently, van der Waals semiconductors have attracted great interest [1-5]. This class of semiconductors are layered materials, composed by two-dimensional (2D) layers bound by interlayer van der Waals forces. Contrary to the case of graphene[6-9], the presence of a bulk band gap favors the achievement of high ON/OFF ratios in field-effect transistors (FETs) with an active channel of 2D semiconductors[10]. These systems, that comprise transition-metal dichalcogenides[11-13], III–VI compounds (InSe, GaSe) [14, 15], and black phosphorus (BP) [16-18], have higher application capabilities compared to graphene. Their layered structure enables easy exfoliation via micromechanical

cleavage[19, 20] or in liquid phase [21-23]. Therefore, van der Waals semiconductors are suitable candidates for applications in optoelectronics[24-26] and flexible electronics[27, 28].

Among van der Waals semiconductors, BP shows charge-carrier mobility as high as 1000 $cm^2/V{\cdot}s$ [29] with an ON/OFF ratio of up to $10^5$ [30], with performances that can even increase upon modification of pristine BP[31] and with potential application also in catalysis[32]. BP is the thermodynamically more stable phase of elemental phosphorus, at ambient pressure and temperature [33] and it is a narrow-gap semiconductor with orthorhombic structure [34], with each layer forming a puckered surface due to $sp^3$ hybridization. Its structural in-plane anisotropy reflects into strongly anisotropic transport[35] and thermal conductivity [36-40]. In addition, the strongly anisotropic band dispersion in the vicinity of the gap implies anisotropic electronic excitations [41]. In BP, the in-plane static screening remains relatively isotropic for momenta relevant to elastic long-range scattering processes [42]. Nonetheless, calculations predict that the band non-parabolicity leads to highly anisotropic plasmons at mid-infrared frequencies[42-45].

Anisotropic electronic properties provide an additional degree of freedom in the design of BP-based optoelectronic nanodevices. Due to its rather low-energy band gap, the anisotropy of optical and electronic properties of BP has been mainly investigated in the near-infrared (NIR) regime[45-47] and only a few works have addressed optical anisotropy in the visible range [48-50], while the ultraviolet (UV) part of the electromagnetic spectrum has not been examined yet. On the other hand, many efforts have recently been dedicated to explore potential applications of plasmon modes in the UV regime[51-55] and it has been demonstrated that BP can enable devising UV photodetectors with photoresponsivity as high as $\sim 9 \times 10^4$ A $W^{-1}$ [56]. One possible advantage of UV plasmons is the matching of their high energy with the electronic transition energy of various biomolecules, thus paving the way for UV plasmonics [52, 57], DNA sensing [58, 59], UV absorbers [60], UV photodetectors[61, 62], UV imaging [63].

It should be noted that gold and silver are the more commonly used materials for plasmonics in the visible range[64], but the imaginary part of their dielectric function assumes rather higher values in the UV range [65]. Therefore, researchers are searching other materials for UV plasmonics [52, 54, 66]. However, one of the crucial issues in UV plasmonics is the limitation of the thickness of native oxide [54]. As an example, the notable efforts for UV plasmonics based on Al[51, 53, 67] have given elusive practical results, since Al suffers the formation of a native oxide layer 3-6 nm thick [68]. Conversely, a stable sub-nanometer (~0.4 nm) layer of $P_2O_5$ forms at the surface of BP exposed to air [69]. Strikingly, the interaction with ambient atmosphere induces only nearly insignificant energy shift (<0.1 eV) in core levels of P atoms[69]. The minimal charge transfer suggests that the native $P_2O_5$ oxide layer on-top of BP is suitable for passivation or as an interface layer for further dielectric deposition.

The above-mentioned peculiarities make BP a suitable candidate for a phosphorus-based UV plasmonics with low cost, wide availability, high conductivity [70], mechanical flexibility [71], and compatibility with complementary metal-oxide semiconductor (CMOS) processing [71]. Moreover, anisotropic metamaterials are strongly desired for the intriguing prospect of scattering-free plasmonic optics [72] and for the possibility to manipulate the polarizations of electromagnetic waves[73].

In this work, we report on the anisotropic UV plasmonic dispersion in BP by means of momentum-resolved electron energy loss spectroscopy (EELS) at atomic resolution and density functional theory (DFT). We find that the excitation spectrum is dominated by an intense mode around 20 eV with anisotropic dispersion, arising from the anisotropy of band structure. Our theoretical model also indicates the presence modes at 0.9 and 2.2 eV, which should be ascribed to single-particle excitations selectively active in the armchair direction. The existence of these features in the excitation spectrum has been validated by high-resolution EELS (HREELS) in reflection.

## 2 Results and discussion

### 2.1 Theoretical model of the excitation spectrum of BP experimentally probed by EELS

Figure 1 shows an experimental high-angle annular dark field scanning transmission electron microscopy (HAADF-STEM) image of BP along the [001] (panel a) crystallographic direction in an AB-stacked BP sample, where P atomic column pairs are directly imaged. The unit cell of BP has an armchair structure along **a** and zigzag along **b.** HAADF-STEM images allow direct determination of the bulk BP lattice parameters, which have been measured to be a=3.31±0.03 Å, b=10.62 ±0.03 Å and c=4.34±0.05 Å (see Electronic Supplementary Information, ESI, Fig. S1 for the identification of structural parameters). These in-plane lattice parameters agree with previous calculations[74-76] and experimental structural investigations [76, 77]. The absence of oxidation is ensured by the analysis of the surface vibrational spectrum probed by HREELS (Fig. S4 in the ESI) and of the $L_{23}$ absorption edge of BP (Figs. S5 and S6 in the ESI).

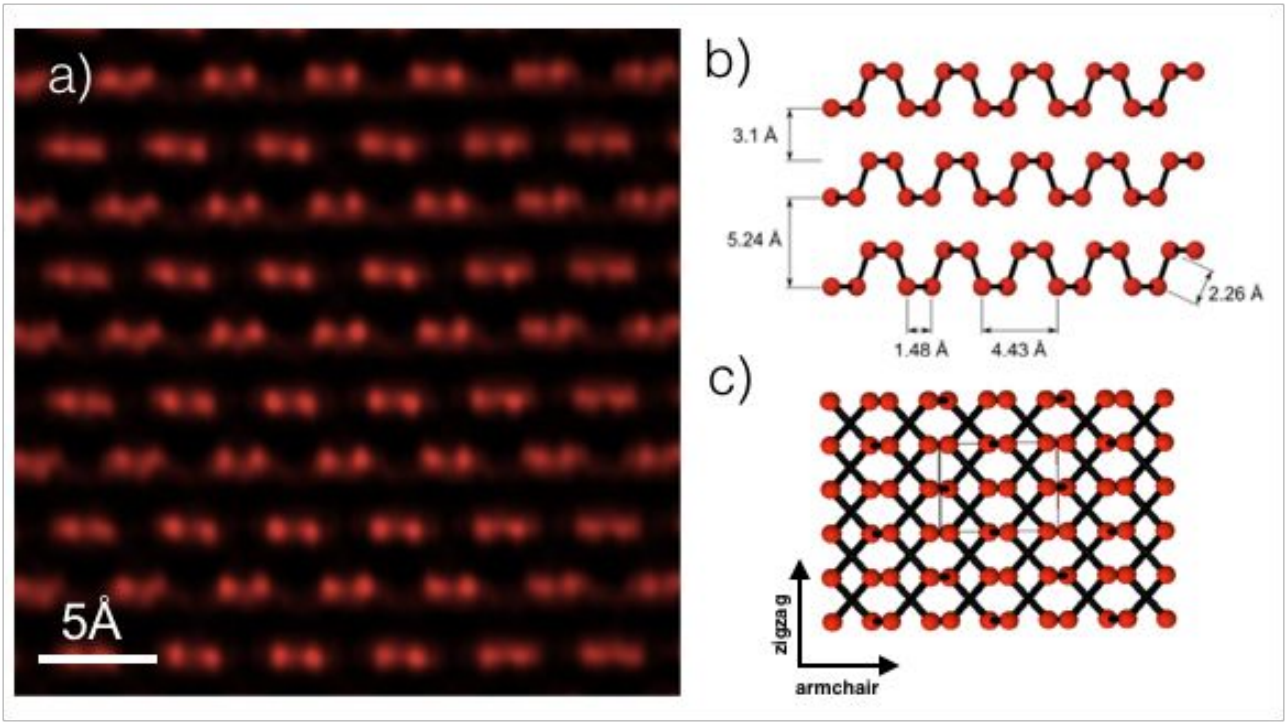

Figure 1: Cross-sectional view (HAADF-STEM images) of bulk BP along the [100] (panel a). In the sketch in panel (b), it is represented that BP atoms are arranged in puckered honeycomb layers, bound together by Van der Waals forces. The armchair (*a* ) and zigzag (*b* ) crystal axis are shown in panel (c).

The low-loss region of EELS spectra (<50 eV) provides information on the dielectric properties of materials and its combination with STEM allows measuring the excitation spectrum with sub-nanometer spatial resolution. The loss function of BP, shown in Figure 2 for a selected momentum of 0.132 $Å^{-1}$, is dominated by an intense peak at ~20 eV, ascribed to a bulk plasmon of BP, in analogy with previous findings[78].

With the aim to cover also the low-energy region (<3 eV) of the excitation spectrum, we have acquired HREELS spectra (with an energy resolution of few meV) in reflection, finding additional modes at 0.9 and 2.2 eV (black curve in Fig. 3). These features are well reproduced by the theoretical loss function (green dots in Fig. 3), calculated using the model discussed below.

The excitation spectrum probed by EELS contains both collective electronic excitations and single-particle transitions from an occupied electronic state to an empty one. Therefore, the inspection of band structure and of the density of states (DOS) is particularly useful for determining the nature of each observed mode. Figure 4 shows the band structure calculated by DFT and the corresponding DOS. Specifically, Fig. 4 reports the bands derived from 3s and 3p orbitals of P, with 8 atoms in the unit cell.

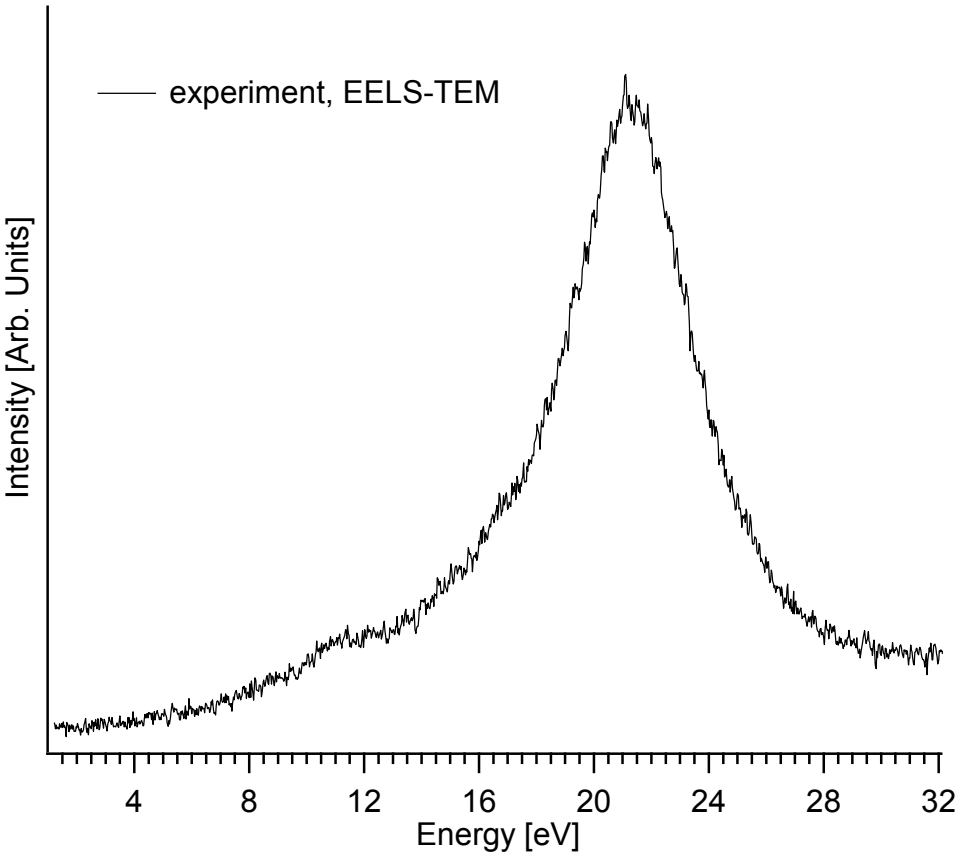


Figure 2: EELS spectrum of BP, acquired in transmission with a primary electron beam energy of 200 keV along the armchair direction. The momentum is 0.132 $Å^{-1}$.

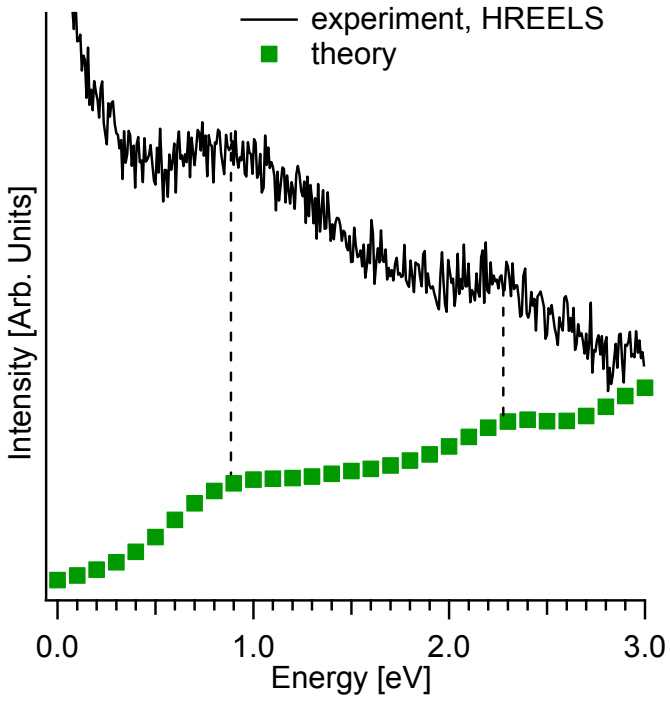

Figure 3: Low-energy excitation spectrum of BP probed by reflection HREELS (black curve), by collecting electrons inelastically scattered by the BP surface. The green dots represent theoretical data.

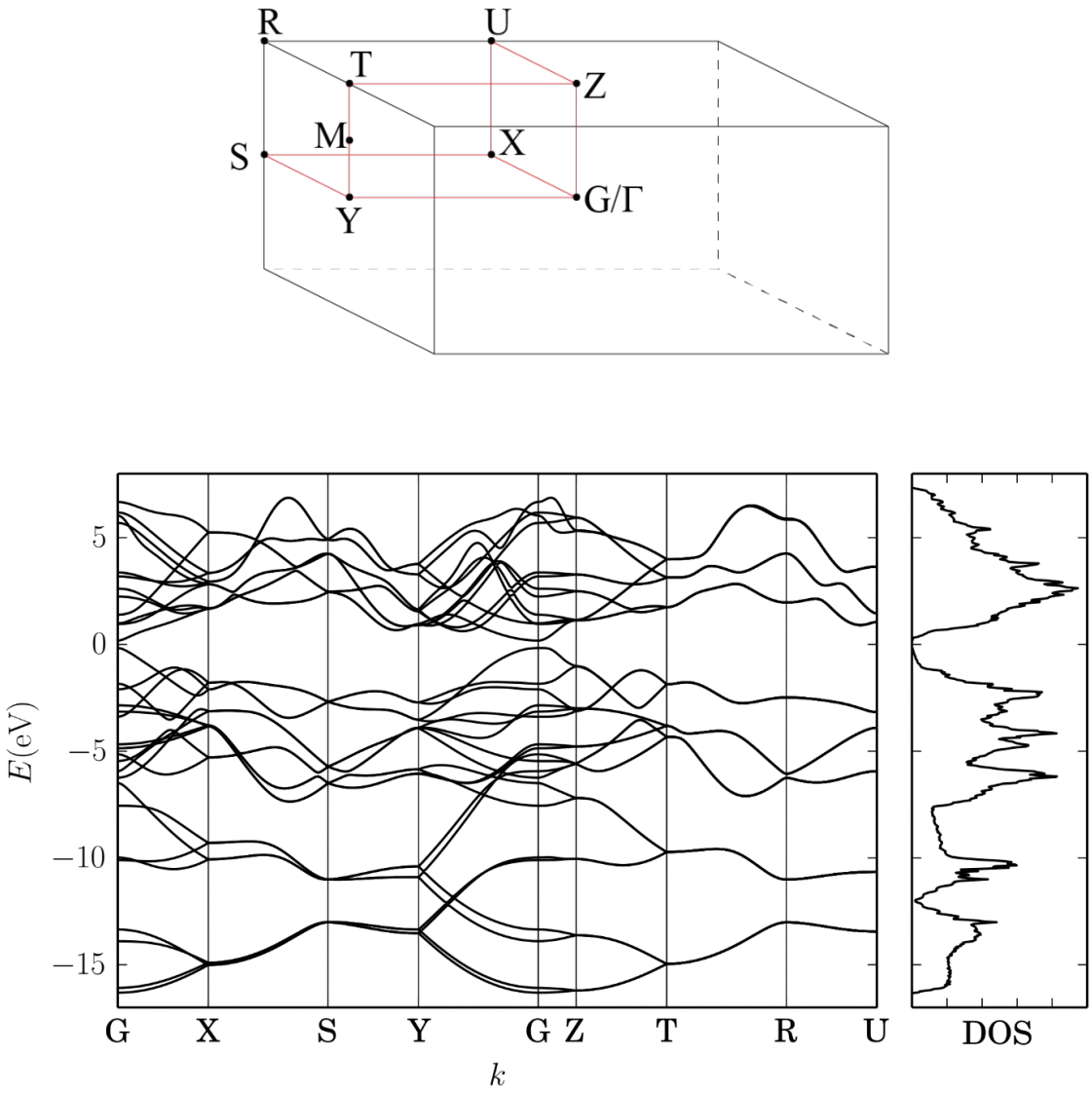


Figure 4. The top panel shows the Brillouin zone of BP. The energy bands of BP along high-symmetry directions are reported in the left part of the bottom panel. These bands are computed from a tight-binding model based on DFT calculations. On the bottom right, the corresponding DOS is reported.

We have evaluated the dielectric function in the plane-wave basis, which is given by [79]

$$\epsilon_{\mathbf{G},\mathbf{G}'}(\mathbf{q},\omega) = \delta_{\mathbf{G},\mathbf{G}'} - \frac{4\pi e^2}{|\mathbf{G}+\mathbf{q}||\mathbf{G}'+\mathbf{q}|}\chi^0_{\mathbf{G},\mathbf{G}'}(\mathbf{q},\omega),$$

with the single-particle response function

$$\chi^0_{\mathbf{G},\mathbf{G}'}(\mathbf{q},\omega) = \frac{1}{(2\pi)^2}\frac{g_s}{\Omega}\sum_{nn'\mathbf{k}}(f_{n'\mathbf{k}+\mathbf{q}} - f_{n\mathbf{k}}) \times \frac{\langle \boldsymbol{\psi}_{n'\mathbf{k}+\mathbf{q}} | e^{-i2\pi(\mathbf{q}+\mathbf{G})\mathbf{r}} | \boldsymbol{\psi}_{n\mathbf{k}} \rangle \langle \boldsymbol{\psi}_{n\mathbf{k}} | e^{-i2\pi(\mathbf{q}+\mathbf{G}')\mathbf{r}} | \boldsymbol{\psi}_{n'\mathbf{k}+\mathbf{q}} \rangle}{E_{n'\mathbf{k}+\mathbf{q}} - E_{n\mathbf{k}} - \omega - i\gamma}$$

Here, the factor $g_s = 2$ is due to spin degeneracy, $\Omega$ is the unit cell area, $f_{n\mathbf{k}}$ is the Fermi-Dirac distribution, $|\boldsymbol{\psi}_{n\mathbf{k}}\rangle$ is an eigenstate with energy $E_{n\mathbf{k}}$, and $\gamma$ is the damping term, which is typically proportional to the imaginary part of the electron self-energy, $\gamma \sim \mathrm{Im}[\Sigma(\omega,\mathbf{k})]$. Since $\Sigma(\omega,\mathbf{k})$ is unknown within the single-particle theory, $\gamma$ is assumed to be a phenomenological parameter, whose value is determined by the details of electron scattering. Taking into account the highly anisotropic character of BP, $\gamma$ could direction-dependent[80]. However, for the purposes of this calculation, we set $\gamma = 0.2$ eV for both directions.

In the calculation of the macroscopic dielectric function, local-field effects are neglected, so that:

$$\epsilon(\mathbf{q},\omega) \approx \varepsilon_{0,0}(\mathbf{q},\omega)$$

The resulting dielectric functions (Fig. 5) indicate the presence of low-energy (< 3 eV) excitations in the armchair direction, as a consequence of the presence of extra features in the band structure in this direction.

**2.2 Dispersion relation of plasmonic modes**

According to dielectric theory [81], plasmon modes exist for frequencies $\omega$ for which $\mathrm{Re}[\epsilon(\mathbf{q},\omega)] = 0$. In the case of BP, $\mathrm{Re}[\epsilon(\mathbf{q},\omega)] = 0$ at ~5 and ~20 eV. The dispersion of the plasmon mode around 20 eV is shown in Figure 7. As for the mode at 5 eV, the imaginary part of the dielectric constant for BP is very large there, and the lifetime (propagation length) of plasmons at ~5 eV is thus short. Conversely, $\mathrm{Im}[\epsilon(\mathbf{q},\omega)]$ is small in the deep-UV range, thus allowing the existence of the plasmon mode at ~20 eV, which predominates the loss function probed by EELS. Contrariwise, the weak shoulder observed in the EELS spectrum around 10 eV (see Fig. 2) corresponds to a single-particle

transition from the $\Gamma_2^+$ band, derived from $p_z$ orbitals, whose wave function has alternating signs between nearest neighbors[82]. Similarly, the two features at 0.9 and 2.2 eV are single-particle excitations selectively active in the armchair direction[83]; we cannot however attribute them to plasmonic modes, due to the fact that the real part of the dielectric function does not cross zero at those energies and the corresponding imaginary part is too high.

Finally, the energy loss function L $(\mathbf{q},\omega)$ (shown in Fig. 6) is computed following:

$$\mathrm{L}\,(\mathbf{q},\omega) = -\mathrm{Im}\left[\frac{1}{\epsilon(\mathbf{q},\omega)}\right]$$

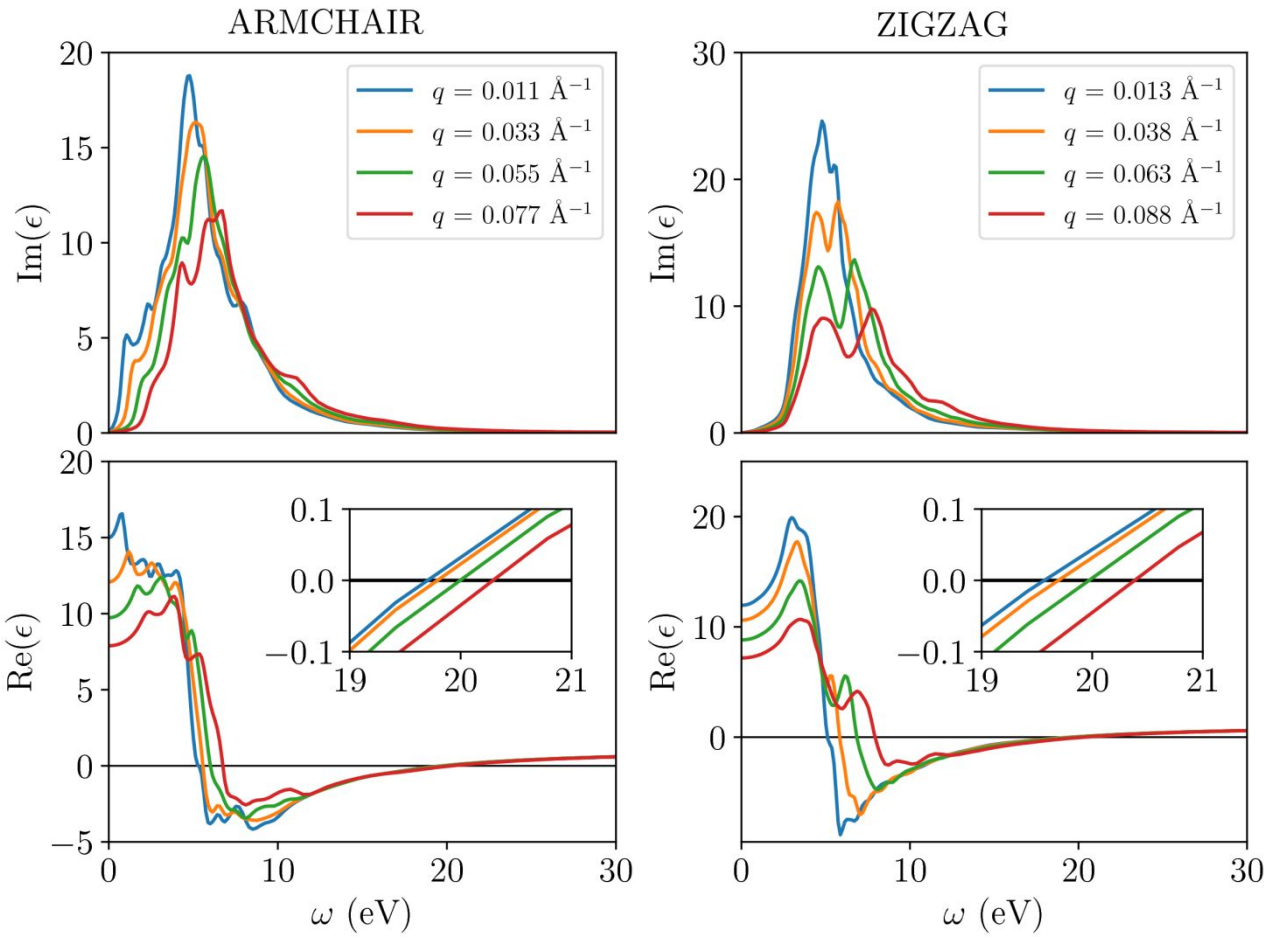


Figure 5. Real and imaginary parts of the theoretically calculated dielectric function as a function of frequency for different momenta $q$ in the (left) armchair and (right) zigzag directions, respectively.

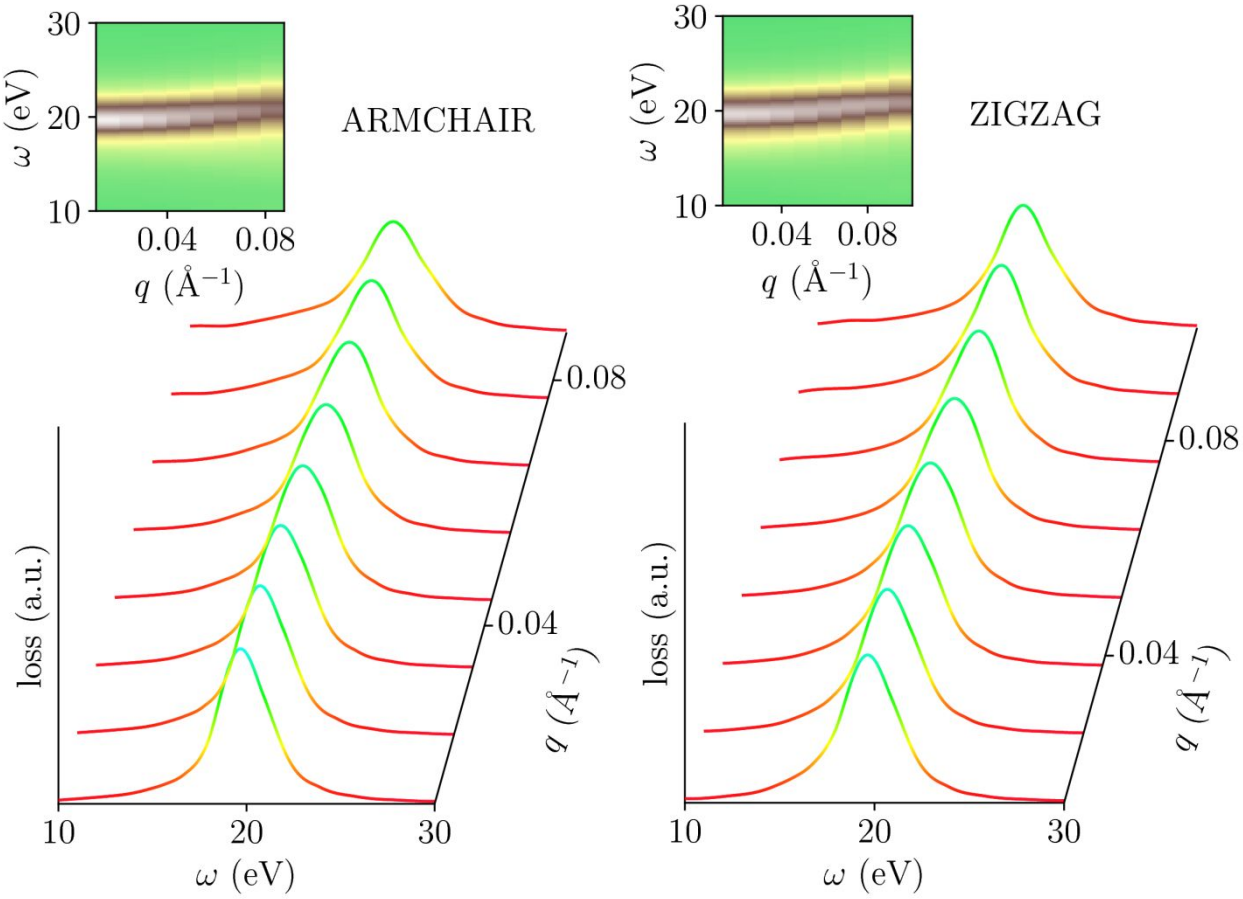


Figure 6. Theoretical loss function computed by DFT for the (left) armchair and (right) zigzag directions. The excitation spectrum is dominated by the intense mode around 20 eV.

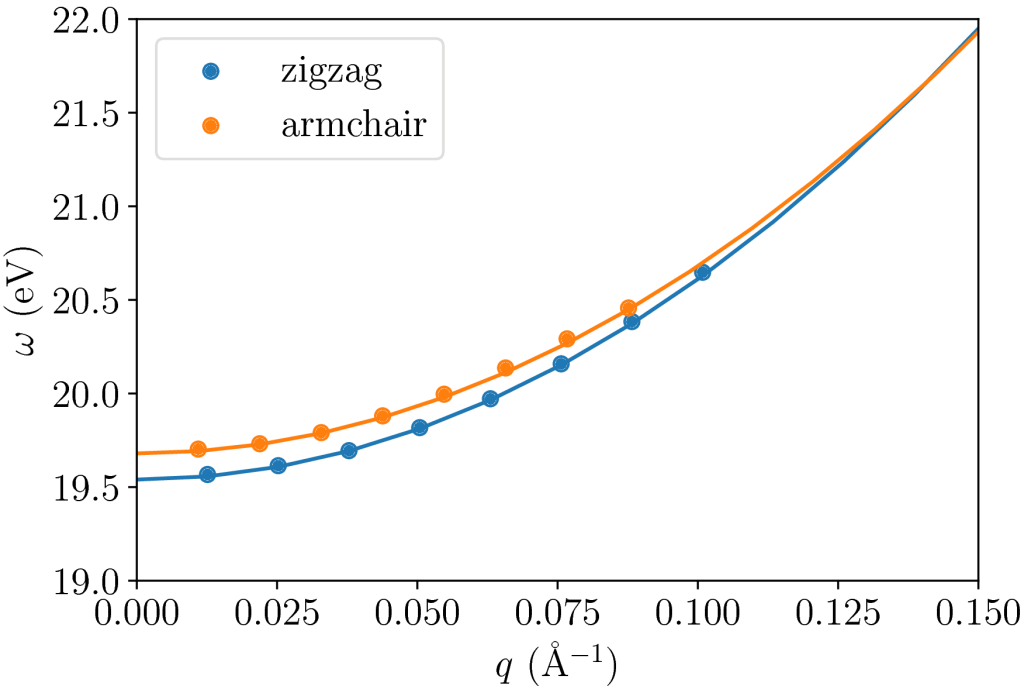

Figure 7. The theoretically calculated plasmon frequency as a function of wave-vector $q$ in both directions, given by $\mathrm{Re}[\epsilon(\mathbf{q},\omega)] = 0$.

Figure 8 shows the experimentally obtained momentum-resolved EELS spectra along the armchair (left panel) and zigzag (right panel) directions, respectively. In the ESI, we also report spectra recorded along the Γ-M direction (Figure S3).

The energy of the plasmon mode at ~20 eV clearly disperses with the momentum $q$, while the scarce intensity of the plasmon at ~10 eV complicates the measurement of its dispersion relation. The dispersion relation (Figure 9), obtained after having extracted the maxima of plasmon spectra, indicates an anisotropic behavior of plasmon dispersion in the deep-UV regime.

Overall, the agreement between the theoretical $\mathrm{L}(\mathbf{q},\omega)$ with experimental data is evident, if we compare Figures 6 and 7 to Figures 8 and 9, respectively.

The dispersion relation has been fitted with a second-order polynomial, as usually done for bulk plasmons:

$$E(q)=E(0)+A\,q^2$$

where E(0) is the plasmon energy at q=0. The values obtained for Γ-M, armchair and zigzag directions are reported in Table I. From this table, it is clear that the anisotropic behavior in $A$ is reproduced by theory, albeit qualitatively. In experiments, the anisotropy is more pronounced, likely due to

anisotropic scattering of plasmons from impurities, phonons, excitons or other scattering sources, that are not included in our theoretical description.

Table I: Fit parameters of the plasmon dispersion along the various directions.

| Direction | Experiment | | Theory | |
|---|---|---|---|---|
| | E(0) [eV] | A [eV·Å$^2$] | E(0) [eV] | A [eV·Å$^2$] |
| Γ-M | 19.6 ± 0.1 | 185 ± 7 | - | - |
| Armchair | 19.6 ± 0.1 | 88 ± 6 | 19.7 | 100 |
| Zigzag | 19.6 ± 0.1 | 154 ± 5 | 19.5 | 107 |

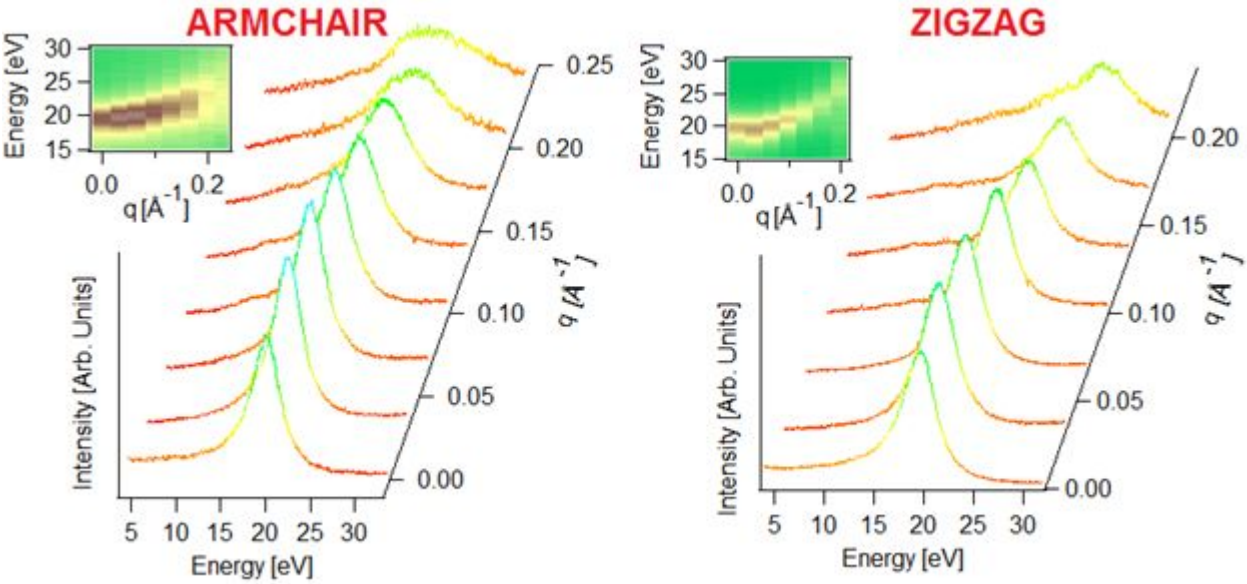


Figure 8: EELS spectra acquired along the armchair and zigzag directions of AB-stacked BP. In the inset, the intensity map is reported

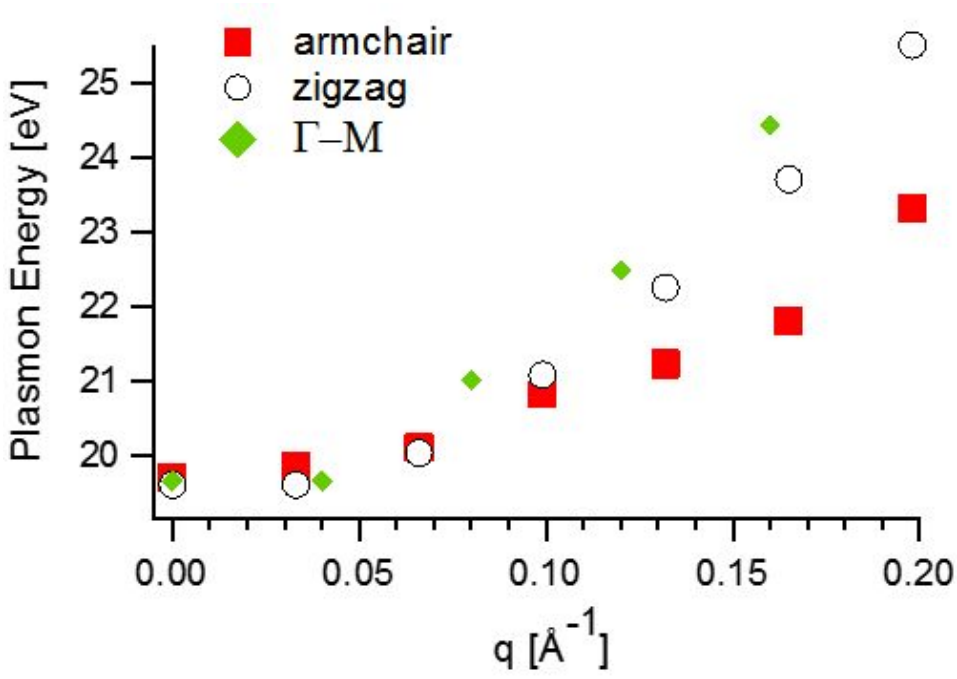


Figure 9: Experimental plasmon dispersion relation in AB-stacked BP

Any layered material is expected to have plasmons showing anisotropic dispersion in the in-plane and out-of-plane directions [84], but BP also exhibits an in-plane anisotropic UV-plasmon dispersion due to its lattice anisotropy in both in-plane and out-of-plane directions, as it could be expected also for BP analogues, such as $ReS_2$ [85]. For the sake of completeness, one should mention that theoretical results also predict anisotropic in-plane UV-plasmon dispersion even for the case of AA-stacked graphite [86], but only far from the long-wavelength limit, where instead UV-plasmon dispersion is isotropic. Conversely, for BP we observe anisotropy even at small momenta.

It is also worth noticing that the anisotropic in-plane UV-plasmon dispersion is expected to occur also for monolayer BP, as previously predicted by *ab initio* time-dependent DFT calculations by Ghosh et al. [44].

In the experimental results, the long-wavelength limit (q~0), the armchair and the zigzag direction have similar plasmon energy, ~19.6 eV, with an energy indetermination given by energy resolution.

However, at higher momenta the dispersion relations along the three directions deviate from each other. For q>0, the plasmon energy in the zigzag direction is always higher than that one in the armchair direction. The energy difference ΔE between the two directions increases with q, reaching ΔE=2.2 eV at q=0.2 $Å^{-1}$. Conversely, in the case of the low-energy plasmon in the THz range, the armchair direction is characterized by higher THz plasmon frequency [42], even if this prediction has not been experimentally confirmed yet.

Materials possessing strong response in the UV spectral range have application capabilities in medicine, ecology, space communication, and in military as flame and missile launching detection Recent works have already demonstrated the role of BP with working wavelength from mid-infrared extending to the UV, and with suppressed dark current by bias voltage [56]. Plasmons, being collective oscillation of charged carriers, open a new route toward enhancing the light-matter interaction. Especially, the existence of UV plasmons in BP opens the way toward the development of UV plasmonic applications based on BP. The anisotropy of the plasmonic dispersion affords tunability to the device, as previously demonstrated for THz photodetectors based on BP [87].

To clarify the application capabilities of the intense UV plasmonic mode at ~20 eV, we introduce a figure of merit, i.e. the quality factor of the plasmon mode $\gamma_p(q) = \omega_p(q)/ \Gamma_p(q)$ [88], where $\Gamma_p(q)$ is the full-width at half-maximum of the plasmon peak of energy $\omega_p(q)$. The value obtained for the mode at ~20 eV, i.e. 4.8, is higher than that estimated for the π-plasmon in graphene (by using data in Refs. [89]), whose application has been recently proposed for sensors for DNA nucleotides [59]. Thus, one can conclude that the technological potential of the plasmonic excitation at ~20 eV in BP is comparable with that of π-plasmon in graphene or even higher.

## Conclusions

We have explored the broadband excitation spectrum of bulk BP by means of a combination of EELS-based techniques, also spatially resolved, and DFT calculations. BP is characterized by an intense

bulk plasmon in the deep-UV regime at ~20 eV, whose dispersion relation is anisotropic. The anisotropic dispersion is reproduced by DFT calculations. The marked anisotropic dispersion of UV-plasmon in BP could enable novel applications of UV plasmonics based on BP. Especially, the properties of plasmonic devices based on BP would depend on the orientation of the BP sample.

Moreover, we reveal the existence of modes at 0.9 and 2.2 eV, which are ascribed to single-particle transitions only active in the armchair direction.

## Acknowledgements

TEM experiments were performed at Beyond-Nano CNR-IMM, which is supported by the Italian Ministry of Education and Research (MIUR) under project Beyond-Nano (PON a3_00363). SY acknowledges financial support from Thousand Young Talent Plan (China). EV acknowledges financial support from the European Research Council Advanced Grant program (Contract No. 338957). AR acknowledges computational facilities of Radboud University (IMM/TCM) funded by the FLAG- ERA JTC2017 Project GRANSPORT. Work at University of Tulane University was supported by the US Department of Energy under Grant No. DE-SC0014208 (support for personnel and material synthesis).

# Methods

### Theoretical methods

Calculations were done on the basis of the projected augmented wave (PAW) method [90] in conjunction with the Perdew-Burke-Ernzerhof (PBE)[91] exchange-correlation functional, as implemented in the Vienna ab-initio simulation package (VASP) [92, 93]. An energy cutoff for the plane-wave expansion was set to 300 eV and the Brillouin zone was sampled by a (20x24x8) k-point mesh. The lattice constants and atomic positions were fully relaxed by keeping the lattice symmetry (point

group $D_{2h}$). The band gap was manually increased by an amount of 0.5 eV to fit the experimentally observed plasmon frequency, so as to correct for DFT band gap underestimation and finite thickness effects.

**Synthesis of BP single crystal**

BP single crystal was grown via chemical vapor transport techniques. A mixture of red phosphorus, AuSn, and $SnI_4$ powder with mole ratio 1000:100:1 was sealed into an evacuated quartz tube. The tube is then placed into a double-zone tube furnace with temperature set at 600 °C and 500 °C for the hot and cold end, respectively. Large single crystals can be obtained after a weeks of transport.

**STEM sample preparation**

Flakes of black-phosphorus have been exfoliated from its bulk and embedded in-between pieces of scrap material in order to create the sandwich for cross-view analysis, which was prepared by standard cross-sectional mechanical polishing. Successively, $Ar^+$ ion milling was carried out with an ion beam energy of 2.5 keV, which has been finally decreased to 0.1 keV for polishing.

**STEM measurements**

Atomic-resolution characterization by TEM was performed through a probe aberration-corrected JEOL ARM200CF, equipped with a Ceos hexapole-type Cs corrector, named CESCOR, and operated at a primary beam energy of 60 keV and 200 keV. The electron gun is a cold-field emission gun with an energy spread of 0.3 eV.

The used installation is capable to deliver a probe size of 0.68 Å at 200 kV, and 1.1 Å at 60 kV. Images were acquired in Z-contrast mode, by using the Gatan HAADF detector with a beam

illumination angle of 33 mrad and a collection angle of 100 mrad. To improve the signal-to-noise ratio of the HAADF-STEM, a low-pass filtering of the images was applied.

**Low-loss EELS measurements**

A fully loaded GIF Quantum ER as EELS spectrometer was used for the EELS measurements, and both low and core-loss EELS spectra were nearly simultaneously acquired by using the DualEELS capability through Gatan Digital Micrograph acquisition software, which also allows the accurate alignment and energy calibration of EELS spectra. The use of Fourier logarithmic deconvolution on a full spectrum obtained by splicing together low- and core-loss EELS allows removing thickness-related plural scattering [94]. The voltage to acquire the low-loss EELS is 200 keV, the convergence semi-angle is 0 mrad (parallel beam), and the collection semi-angle is 5 mrad.

**Q-resolved EELS (q-EELS) measurements**

All momentum-resolved electron energy-loss (q-EELS) measurements with TEM were performed at 200 kV under diffraction mode, with parallel beam illumination. The EELS spectrometer was set to 0.05 eV dispersion, yielding an energy resolution of 0.65 eV. Such an energy resolution is sufficient to reveal different features in the low-loss region of the spectra. Acquisition was carried out with a fixed exposure time of 0.4 s. All experiments have been carried out at room temperature.

**HREELS**

HREELS experiments in the low-energy region were carried out by using a Delta 0.5 spectrometer by SPECS GmbH at University of Calabria, Italy. The experimental resolution is 0.003 eV. The

primary electron beam energy is 20 eV. HREELS experiments have been carried out at room temperature with incidence and scattering angles fixed at 55° with respect to the sample normal.

## REFERENCES


1. J. Koo, S. Gao, H. Lee and L. Yang, *Nanoscale*, 2017, **9**, 14540-14547.
2. A. Arora, M. Drüppel, R. Schmidt, T. Deilmann, R. Schneider, M. R. Molas, P. Marauhn, S. Michaelis De Vasconcellos, M. Potemski, M. Rohlfing and R. Bratschitsch, *Nat. Commun.*, 2017, **8**.
3. L. Ottaviano, S. Palleschi, F. Perrozzi, G. D'Olimpio, F. Priante, M. Donarelli, P. Benassi, M. Nardone, M. Gonchigsuren, M. Gombosuren, A. Lucia, G. Moccia and O. A. Cacioppo, *2D Mater.*, 2017, **4**.
4. M. Donarelli, S. Prezioso, F. Perrozzi, F. Bisti, M. Nardone, L. Giancaterini, C. Cantalini and L. Ottaviano, *Sens. Actuators B: Chem.*, 2015, **207**, 602-613.
5. M. Donarelli, F. Perrozzi, F. Bisti, F. Paparella, V. Feyer, A. Ponzoni, M. Gonchigsuren and L. Ottaviano, *Nanoscale*, 2015, **7**, 11453-11459.
6. K. Novoselov, *Nat. Mater.*, 2007, **6**, 720-721.
7. A. Cupolillo, N. Ligato and L. S. Caputi, *Appl. Phys. Lett.*, 2013, **102**, 111609-111604.
8. A. Cupolillo, N. Ligato and L. Caputi, *Surf. Sci.*, 2013, **608**, 88-91.
9. A. Cupolillo, N. Ligato and L. S. Caputi, *Carbon*, 2012, **50**, 2588-2591.
10. C. Wang, Q. He, U. Halim, Y. Liu, E. Zhu, Z. Lin, H. Xiao, X. Duan, Z. Feng, R. Cheng, N. O. Weiss, G. Ye, Y. C. Huang, H. Wu, H. C. Cheng, I. Shakir, L. Liao, X. Chen, W. A. Goddard, Y. Huang and X. Duan, *Nature*, 2018, **555**, 231-236.
11. I. S. Kwon, I. H. Kwak, H. G. Abbas, G. Jung, Y. Lee, J. Park, S. J. Yoo, J. G. Kim and H. S. Kang, *Nanoscale*, 2018, **10**, 11349-11356.
12. W. T. Kang, I. M. Lee, S. J. Yun, Y. I. Song, K. Kim, D. H. Kim, Y. S. Shin, K. Lee, J. Heo, Y. M. Kim, Y. H. Lee and W. J. Yu, *Nanoscale*, 2018, **10**, 11397-11402.
13. F. Perrozzi, S. M. Emamjomeh, V. Paolucci, G. Taglieri, L. Ottaviano and C. Cantalini, *Sens. Actuators, B*, 2017, **243**, 812-822.
14. Y. Sun, S. Luo, X. G. Zhao, K. Biswas, S. L. Li and L. Zhang, *Nanoscale*, 2018, **10**, 7991-7998.
15. Q. Li, Y. Zhao, J. Guo, Q. Zhou, Q. Chen and J. Wang, *Nanoscale*, 2018, **10**, 3799-3804.
16. P. Zereshki, Y. Wei, F. Ceballos, M. Z. Bellus, S. D. Lane, S. Pan, R. Long and H. Zhao, *Nanoscale*, 2018, **10**, 11307-11313.
17. N. Goyal, N. Kaushik, H. Jawa and S. Lodha, *Nanoscale*, 2018, **10**, 11616-11623.
18. M. Donarelli, L. Ottaviano, L. Giancaterini, G. Fioravanti, F. Perrozzi and C. Cantalini, *2D Mater.*, 2016, **3**, 025002.
19. A. H. Woomer, T. W. Farnsworth, J. Hu, R. A. Wells, C. L. Donley and S. C. Warren, *ACS Nano*, 2015, **9**, 8869–8884.
20. Y. Chen, G. Jiang, S. Chen, Z. Guo, X. Yu, C. Zhao, H. Zhang, Q. Bao, S. Wen, D. Tang and D. Fan, *Opt. Express*, 2015, **23**, 12823-12833.
21. J. Kang, J. D. Wood, S. A. Wells, J.-H. Lee, X. Liu, K.-S. Chen and M. C. Hersam, *ACS Nano*, 2015, **9**, 3596–3604.
22. Z. Guo, H. Zhang, S. Lu, Z. Wang, S. Tang, J. Shao, Z. Sun, H. Xie, H. Wang, X.-F. Yu and P. K. Chu, *Adv. Funct. Mater.*, 2015, **25**, 6996–7002.
23. X. Zhang, H. Xie, Z. Liu, C. Tan, Z. Luo, H. Li, J. Lin, L. Sun, W. Chen, Z. Xu, L. Xie, W. Huang and H. Zhang, *Angew. Chem.*, 2015, **54**, 3653–3657.
24. G. Eda and S. A. Maier, *ACS Nano*, 2013, **7**, 5660-5665.
25. F. Xia, H. Wang and Y. Jia, *Nat. Commun.*, 2014, **5**, 4458.
26. S. Lei, F. Wen, B. Li, Q. Wang, Y. Huang, Y. Gong, Y. He, P. Dong, J. Bellah, A. George, L. Ge, J. Lou, N. J. Halas, R. Vajtai and P. M. Ajayan, *Nano Lett.*, 2015, **15**, 259-265.
27. D. Akinwande, N. Petrone and J. Hone, *Nat. Commun.*, 2014, **5**, 5678.

28. Q. Wang, K. Xu, Z. Wang, F. Wang, Y. Huang, M. Safdar, X. Zhan, F. Wang, Z. Cheng and J. He, *Nano Lett.*, 2015, **15**, 1183-1189.
29. H. Hu, H. Gao, L. Gao, F. Li, N. Xu, X. Long, Y. Hu, J. Jin and J. Ma, *Nanoscale*, 2018, **10**, 5834-5839.
30. S. Yang, K. Zhang, G. Ricciardulli Antonio, P. Zhang, Z. Liao, R. Lohe Martin, E. Zschech, W. M. Blom Paul, W. Pisula, K. Müllen and X. Feng, *Angew. Chem.*, 2018, **130**, 4767-4771.
31. Z. Guo, S. Chen, Z. Wang, Z. Yang, F. Liu, Y. Xu, J. Wang, Y. Yi, H. Zhang, L. Liao, P. K. Chu and X.-F. Yu, *Adv. Mater.*, 2017, **29**, 1703811.
32. Q. Jiang, L. Xu, N. Chen, H. Zhang, L. Dai and S. Wang, *Angew. Chem.*, 2016, **55**, 13849-13853.
33. H. Liu, Y. Du, Y. Deng and P. D. Ye, *Chem. Soc. Rev.*, 2015, **44**, 2732-2743.
34. W. Lei, G. Liu, J. Zhang and M. Liu, *Chem. Soc. Rev.*, 2017, **46**, 3492-3509.
35. A. Mishchenko, Y. Cao, G. L. Yu, C. R. Woods, R. V. Gorbachev, K. S. Novoselov, A. K. Geim and L. S. Levitov, *Nano Lett.*, 2015, **15**, 6991-6995.
36. H. Jang, J. D. Wood, C. R. Ryder, M. C. Hersam and D. G. Cahill, *Adv. Mater.*, 2015, **27**, 8017–8022.
37. S. Lee, F. Yang, J. Suh, S. Yang, Y. Lee, G. Li, H. Sung Choe, A. Suslu, Y. Chen, C. Ko, J. Park, K. Liu, J. Li, K. Hippalgaonkar, J. J. Urban, S. Tongay and J. Wu, *Nat. Commun.*, 2015, **6**, 8573.
38. S. G. Jeon, H. Shin, Y. H. Jaung, J. Ahn and J. Y. Song, *Nanoscale*, 2018, **10**, 5985-5989.
39. B. Sun, X. Gu, Q. Zeng, X. Huang, Y. Yan, Z. Liu, R. Yang and Y. K. Koh, *Adv. Mater.*, 2017, **29**.
40. B. Smith, B. Vermeersch, J. Carrete, E. Ou, J. Kim, N. Mingo, D. Akinwande and L. Shi, *Adv. Mater.*, 2017, **29**.
41. A. S. Rodin, A. Carvalho and A. H. Castro Neto, *Phys. Rev. Lett.*, 2014, **112**, 176801.
42. T. Low, R. Roldán, H. Wang, F. Xia, P. Avouris, L. M. Moreno and F. Guinea, *Phys. Rev. Lett.*, 2014, **113**, 106802.
43. D. T. Debu, S. J. Bauman, D. French, H. O. Churchill and J. B. Herzog, *Sci. Rep.*, 2018, **8**, 3224.
44. B. Ghosh, P. Kumar, A. Thakur, Y. S. Chauhan, S. Bhowmick and A. Agarwal, *Phys. Rev. B*, 2017, **96**, 035422.
45. I.-H. Lee, L. Martin-Moreno, D. A. Mohr, K. Khaliji, T. Low and S.-H. Oh, *ACS Photonics*, 2018, **5**, 2208-2216.
46. T. Hong, B. Chamlagain, W. Lin, H. J. Chuang, M. Pan, Z. Zhou and Y. Q. Xu, *Nanoscale*, 2014, **6**, 8978-8983.
47. S. Ge, C. Li, Z. Zhang, C. Zhang, Y. Zhang, J. Qiu, Q. Wang, J. Liu, S. Jia, J. Feng and D. Sun, *Nano Lett.*, 2015, **15**, 4650-4656.
48. N. Mao, J. Tang, L. Xie, J. Wu, B. Han, J. Lin, S. Deng, W. Ji, H. Xu, K. Liu, L. Tong and J. Zhang, *J. Am. Chem. Soc.*, 2016, **138**, 300-305.
49. J. Nong, W. Wei, W. Wang, G. Lan, Z. Shang, J. Yi and L. Tang, *Opt. Express*, 2018, **26**, 1633-1644.
50. C. Zhao, M. C. Sekhar, W. Lu, C. Zhang, J. Lai, S. Jia and D. Sun, *Nanotechnology*, 2018, **29**, 245202.
51. M. W. Knight, N. S. King, L. Liu, H. O. Everitt, P. Nordlander and N. J. Halas, *ACS Nano*, 2014, **8**, 834-840.
52. J. M. McMahon, G. C. Schatz and S. K. Gray, *Phys. Chem. Chem. Phys.*, 2013, **15**, 5415-5423.
53. F. Bisio, R. Proietti Zaccaria, R. Moroni, G. Maidecchi, A. Alabastri, G. Gonella, A. Giglia, L. Andolfi, S. Nannarone, L. Mattera and M. Canepa, *ACS Nano*, 2014, **8**, 9239-9247.
54. A. M. Watson, X. Zhang, R. Alcaraz de la Osa, J. M. Sanz, F. González, F. Moreno, G. Finkelstein, J. Liu and H. O. Everitt, *Nano Lett.*, 2015, **15**, 1095-1100.
55. J.-Y. Ou, J.-K. So, G. Adamo, A. Sulaev, L. Wang and N. I. Zheludev, *Nat. Commun.*, 2014, **5**, 5139.
56. J. Wu, G. K. W. Koon, D. Xiang, C. Han, C. T. Toh, E. S. Kulkarni, I. Verzhbitskiy, A. Carvalho, A. S. Rodin and S. P. Koenig, *ACS Nano*, 2015, **9**, 8070-8077.
57. M. P. Knudson, A. J. Hryn, M. D. Huntington and T. W. Odom, *ACS Appl. Mater. Interfaces*, 2017, **9**, 33554-33558.
58. A. Taguchi, Y. Saito, K. Watanabe, S. Yijian and S. Kawata, *Appl. Phys. Lett.*, 2012, **101**, 081110.
59. B. Fotouhi, V. Ahmadi, M. Abasifard and R. Roohi, *J. Phys. Chem. C*, 2016, **120**, 13693–13700.
60. Y. E. Kesim, E. Battal and A. K. Okyay, *AIP Advances*, 2014, **4**, 077106.
61. S. C. Dhanabalan, J. S. Ponraj, H. Zhang and Q. Bao, *Nanoscale*, 2016, **8**, 6410-6434.

62. J. S. Ponraj, Z.-Q. Xu, S. C. Dhanabalan, H. Mu, Y. Wang, J. Yuan, P. Li, S. Thakur, M. Ashrafi, K. Mccoubrey, Y. Zhang, S. Li, H. Zhang and Q. Bao, *Nanotechnology*, 2016, **27**, 462001.
63. Z. Xinyu, W. Keyi, M. Jiajun, Z. Qijin, Y. Peizheng and T. Xiujie, *Photonics Technology Letters, IEEE*, 2015, **27**, 1297-1300.
64. E. Ozbay, *Science*, 2006, **311**, 189-193.
65. A. Politano and G. Chiarello, *Prog. Surf. Sci.*, 2015, **90**, 144-193.
66. Y. Wang, E. M. Peterson, J. M. Harris, K. Appusamy, S. Guruswamy and S. Blair, *J. Phys. Chem. C*, 2017, **121**, 11650-11657.
67. C. Forestiere, A. Handin and L. Dal Negro, *Plasmonics*, 2014, **9**, 715-725.
68. J. Evertsson, F. Bertram, F. Zhang, L. Rullik, L. R. Merte, M. Shipilin, M. Soldemo, S. Ahmadi, N. Vinogradov, F. Carlà, J. Weissenrieder, M. Göthelid, J. Pan, A. Mikkelsen, J. O. Nilsson and E. Lundgren, *Appl. Surf. Sci.*, 2015, **349**, 826-832.
69. M. T. Edmonds, A. Tadich, A. Carvalho, A. Ziletti, K. M. O'Donnell, S. P. Koenig, D. F. Coker, B. Özyilmaz, A. H. C. Neto and M. S. Fuhrer, *ACS Appl. Mater. Interfaces*, 2015, **7**, 14557–14562.
70. J. Qiao, X. Kong, Z. X. Hu, F. Yang and W. Ji, *Nat. Commun.*, 2014, **5**, 4475.
71. W. Zhu, M. N. Yogeesh, S. Yang, S. H. Aldave, J.-S. Kim, S. Sonde, L. Tao, N. Lu and D. Akinwande, *Nano Lett.*, 2015, **15**, 1883-1890.
72. J. Elser and V. A. Podolskiy, *Phys. Rev. Lett.*, 2008, **100**, 066402.
73. J. Hao, Y. Yuan, L. Ran, T. Jiang, J. A. Kong, C. T. Chan and L. Zhou, *Phys. Rev. Lett.*, 2007, **99**, 063908.
74. J. Dai and X. C. Zeng, *J. Phys. Chem. Lett.*, 2014, **5**, 1289-1293.
75. Y. Li, S. Yang and J. Li, *J. Phys. Chem. C*, 2014, **118**, 23970-23976.
76. G. Nicotra, A. Politano, A. M. Mio, I. Deretzis, J. Hu, Z. Q. Mao, J. Wei, A. La Magna and C. Spinella, *Phys. Status Solidi B*, 2016, **253**, 2509-2514.
77. R. J. Wu, M. Topsakal, T. Low, M. C. Robbins, N. Haratipour, J. S. Jeong, R. M. Wentzcovitch, S. J. Koester and K. A. Mkhoyan, *J. Vac. Sci. Technol. A*, 2015, **33**, 060604.
78. A. Morita, *Appl. Phys. A*, 1986, **39**, 227-242.
79. M. Gajdoš, K. Hummer, G. Kresse, J. Furthmüller and F. Bechstedt, *Phys. Rev. B*, 2006, **73**, 045112.
80. A. Rudenko, S. Brener and M. Katsnelson, *Phys. Rev. Lett.*, 2016, **116**, 246401.
81. A. Liebsch, *Electronic Excitations at Metal Surfaces*, Plenum, New York, 1997.
82. Y. Takao, H. Asahina and A. Morita, *J. Phys. Soc. Jpn.*, 1981, **50**, 3362-3369.
83. R. Schuster, J. Trinckauf, C. Habenicht, M. Knupfer and B. Büchner, *Phys. Rev. Lett.*, 2015, **115**, 026404.
84. K. Zeppenfeld, *Phys. Lett. A*, 1967, **25**, 335-336.
85. M. Rahman, K. Davey and S. Z. Qiao, *Adv. Funct. Mater.*, 2017, **27**.
86. C.-W. Chiu, F.-L. Shyu, M.-F. Lin, G. Gumbs and O. Roslyak, *J. Phys. Soc. Jpn.*, 2012, **81**, 104703.
87. L. Viti, J. Hu, D. Coquillat, A. Politano, W. Knap and M. S. Vitiello, *Sci. Rep.*, 2016, **6**, 20474.
88. A. Principi, G. Vignale, M. Carrega and M. Polini, *Phys. Rev. B*, 2013, **88**, 195405.
89. A. Politano, I. Radović, D. Borka, Z. L. Mišković and G. Chiarello, *Carbon*, 2016, **96**, 91-97.
90. P. E. Blöchl, *Phys. Rev. B*, 1994, **50**, 17953-17979.
91. J. P. Perdew, K. Burke and M. Ernzerhof, *Phys. Rev. Lett.*, 1996, **77**, 3865-3868.
92. G. Kresse and J. Furthmüller, *Phys. Rev. B*, 1996, **54**, 11169-11186.
93. G. Kresse and D. Joubert, *Phys. Rev. B*, 1999, **59**, 1758.
94. J. Scott, P. J. Thomas, M. MacKenzie, S. McFadzean, J. Wilbrink, A. J. Craven and W. A. P. Nicholson, *Ultramicroscopy*, 2008, **108**, 1586-1594.